Graphene based plasmonic terahertz amplitude modulator operating above 100 MHz

D. S. Jessop, S. J. Kindness, L. Xiao, P. Braeuninger-Weimer, H. Lin, Y. Ren, C. X. Ren, S. Hofmann, J. A. Zeitler, H. E. Beere, D. A. Ritchie, and R. Degl'Innocenti

Citation: Applied Physics Letters **108**, 171101 (2016); doi: 10.1063/1.4947596
View online: http://dx.doi.org/10.1063/1.4947596
View Table of Contents: http://scitation.aip.org/content/aip/journal/apl/108/17?ver=pdfcov
Published by the AIP Publishing

Graphene based plasmonic terahertz amplitude modulator operating above 100 MHz

D. S. Jessop,[1,a)] S. J. Kindness,[1] L. Xiao,[2] P. Braeuninger-Weimer,[2] H. Lin,[3,b)] Y. Ren,[1] C. X. Ren,[4] S. Hofmann,[2] J. A. Zeitler,[3] H. E. Beere,[1] D. A. Ritchie,[1] and R. Degl'Innocenti[1,a)]

[1]*Cavendish Laboratory, University of Cambridge, J J Thomson Avenue, Cambridge CB3 0HE, United Kingdom*

[2]*Department of Engineering, University of Cambridge, 9 J J Thomson Avenue, Cambridge CB3 0FA, United Kingdom*

[3]*Department of Chemical Engineering & Biotechnology, University of Cambridge, Pembroke Street, Cambridge CB2 3RA, United Kingdom*

[4]*Department of Materials Science and Metallurgy, University of Cambridge, 27 Charles Babbage Road, Cambridge CB3 0FS, United Kingdom*

(Received 11 March 2016; accepted 14 April 2016; published online 26 April 2016)

The terahertz (THz) region of the electromagnetic spectrum holds great potential in many fields of study, from spectroscopy to biomedical imaging, remote gas sensing, and high speed communication. To fully exploit this potential, fast optoelectronic devices such as amplitude and phase modulators must be developed. In this work, we present a room temperature external THz amplitude modulator based on plasmonic bow-tie antenna arrays with graphene. By applying a modulating bias to a back gate electrode, the conductivity of graphene is changed, which modifies the reflection characteristics of the incoming THz radiation. The broadband response of the device was characterized by using THz time-domain spectroscopy, and the modulation characteristics such as the modulation depth and cut-off frequency were investigated with a 2.0 THz single frequency emission quantum cascade laser. An optical modulation cut-off frequency of 105 ± 15 MHz is reported. The results agree well with a lumped element circuit model developed to describe the device.
[http://dx.doi.org/10.1063/1.4947596]

The terahertz (THz) or sub-millimeter region of the electromagnetic spectrum (0.3–10 THz) has attracted great interest in recent years in many different physical fields such as spectroscopy,[1] imaging,[2,3] security,[4] medical diagnosis,[5] and wireless communication.[6] In the field of spectroscopy, external THz amplitude, phase and frequency modulators would further justify the use of THz quantum cascade lasers (QCLs). For communication, the THz region offers a broad, unutilized spectrum, with many demonstrations of high-speed communication at sub-THz and low-THz frequencies.[7,8] To be a commercially viable next generation technology, efficient, high-speed, external amplitude, frequency and phase modulation of THz radiation using optoelectronic devices must be developed.

Graphene offers a superior solution to the field of THz modulation, due to its remarkable properties such as high carrier mobility[9] and large achievable charge carrier densities.[10] Graphene is also attractive from a processing perspective, as it is compatible with many existing semiconductor processes. Several authors have already incorporated graphene into external THz modulators[11–13] but have been limited in cut-off frequency by the large areas of graphene and the architectures used. Recently, graphene was directly integrated onto a THz QCL and achieved 100% modulation depth with a modulation speed over 100 MHz.[14] For use in communications, detaching the modulator and source and utilizing external modulation allow single QCL sources to be used, with the advantage that a single source is able to generate a frequency and phase stable set of independent quadrature signals for modulation.

To enhance graphene based modulators, plasmonic/metamaterial based devices are attracting a large amount of attention. These materials provide strong confinement of electromagnetic radiation at a designed frequency, which can span many orders of magnitude.[15,16] Recent work in the mid-infrared using metamaterials/plasmonics with graphene has demonstrated up to 20% frequency modulation at speeds greater than 30 MHz (Ref. 17) and 30% amplitude modulation at 40 MHz.[18] Further, the same group demonstrated 100% modulation depth with a theoretical modulation speed of 20 GHz, using a Fabry–Pérot enhanced absorber with a graphene/metasurface tunable mirror.[19]

In this paper, we present a room temperature, external optoelectronic amplitude modulator, centered around 2.0 THz. The device uses graphene to actively shunt an array of bow-tie antennas, enabling modulation of incoming THz radiation generated by a 2.0 THz single frequency emission QCL. The device consists of four arrays of bow-tie antennas, with each array characterized by the length of the antenna (L), which determines the resonant frequency of the antenna array. Between the gap of each antenna is a small graphene rectangle that provides a variable shunt resistance between

[a)]Authors to whom correspondence should be addressed. Electronic addresses: dsj23@cam.ac.uk and rd448@cam.ac.uk.
[b)]Now at Department of Engineering, Lancaster University, Lancaster LA1 4YW, United Kingdom.

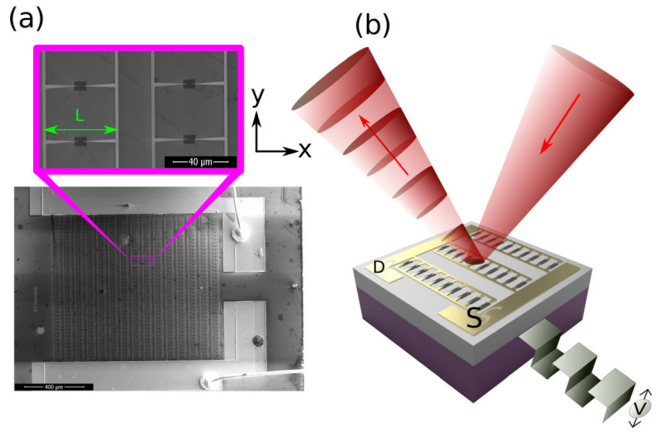

FIG. 1. (a) Scanning electron microscope image of the device. The graphene rectangles are clearly visible between the arms of the antennas. (b) Schematic of the device. A modulating signal to the back gate causes modulation on incoming THz radiation. Source and drain electrodes are grounded.

the arms. Electrically connecting the antennas to source/drain electrodes by perpendicular metallic strips results in a conductive path for the graphene to charge/discharge. By electrostatically doping the graphene, the shunt resistance is changed, and hence, the electromagnetic response of the array changes, leading to optoelectronic modulation. Optical measurements show a cut-off frequency above 100 MHz, in good agreement with a lumped circuit model developed to describe the device.

The substrate used for the device was a $525 \pm 25\,\mu$m thick p-Si (Boron doped) with a resistivity of $20 \pm 5\ \Omega \cdot$cm and 300 ± 25 nm thick thermal oxide. The large area graphene was fabricated and transferred to the substrate using a similar process as described in Refs. 20 and 21. The graphene rectangles were defined via electron beam lithography and O_2 plasma etching, while the antennas were processed via two stages of electron beam lithography and thermal evaporation. Four arrays with $L = \{47, 48, 49, 51\}$ μm, corresponding to resonant frequencies f_{res} around 2.0 THz, were processed onto one chip, allowing for coarse tuning of the resonant frequency in order to account for possible differences between simulation and experiment. The fully processed device was then mounted in a Au-ceramic chip carrier with conductive Ag adhesive, allowing back gate electrical contact through the p-Si substrate. The source and drain pads for each array were Au wire bonded to different pins of the Au-ceramic chip carrier.

Figure 1(a) shows a scanning electron microscope image of a device with $L = 51\,\mu$m along with a schematic shown in Fig. 1(b). The bow-tie antennas have a flare angle of 5° and a gap between the two arms of 2 μm. The graphene rectangles between the arms have an area of $8 \times 4\,\mu\text{m}^2$. The pitch between adjacent antennas in the x and y directions are 1.55·L and 0.33·L, respectively. In total, 15 columns and 41 rows of antennas covering a total area of $1 \times 1.2\,\text{mm}^2$ were defined. The two metallic antenna arms are nominally 60 nm of Pd and 60 nm of Ti, both capped with a 15 nm layer of Au. For the purpose of modulation, this bimetallic design does not significantly affect performance but opens upon the possibility of detection.[22]

To simulate the spectral response of the device, we employed the commercial software COMSOL Multiphysics® v 5.1. A single unit cell was modelled with periodic boundary conditions. The optical properties of the materials were defined via the complex permittivity ε_r, with the SiO_2 layer defined as $\varepsilon_r = 3.9$ and the graphene, Pd, Ti, and p-Si described by the Drude model.[23,24] A plane wave with an electric field polarization along the antenna length is excited by a port boundary condition which is also used to monitor the reflected power. Figure 2(a) shows the spectral reflectivity for the $L = 51\,\mu$m device at different graphene sheet conductivities (σ_G^S). A clear modulation of the reflected light is observed with the maximum modulation depth seen at the resonant frequency $f_{res} \sim 2$ THz. Figure 2(b) shows that the resonance is tunable by acting on the antenna length L, with an approximate $f_{res} \propto 1/L$ relationship as expected.[25,26] As expected, when the incident THz radiation is polarized perpendicular to the antenna's major axis, no resonant features are observed, only a Drude like response at low frequencies. Also, due to the small area of graphene on this device, there is no appreciable modulation away from resonance as σ_G^S is changed. Figure 2(c) presents the simulated reflectivity spectrum for the $L = 51\,\mu$m array along with the measured reflectivity spectrum from a commercial THz time-domain spectroscopy (THz-TDS) system (Imaga 2000 from Teraview,

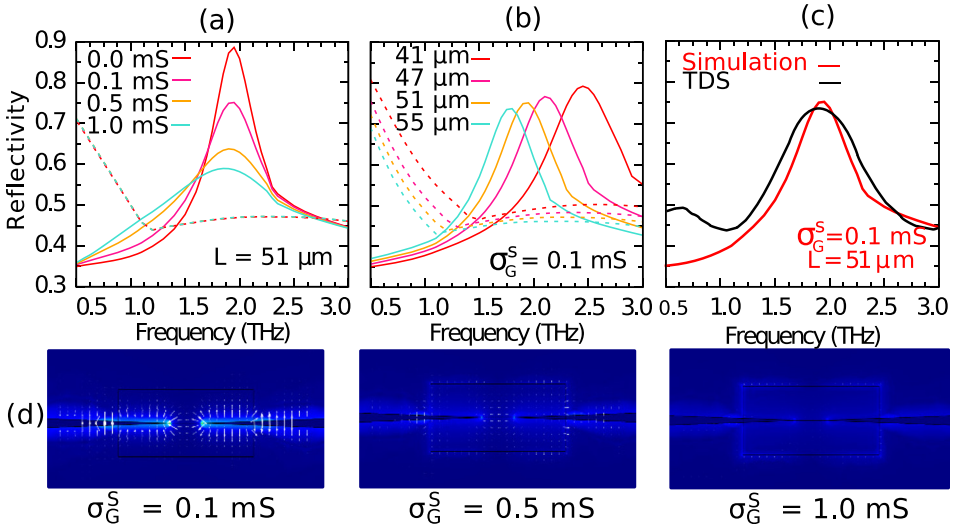

FIG. 2. Simulated spectral reflectivity of the device for THz radiation polarized both parallel (solid line) and perpendicular (dashed line) to the antenna major axis. (a) Spectral reflectivity for different σ_G^S. (b) Spectral reflectivity for different L. (c) Measured spectral reflectivity and simulated spectral reflectivity. (d) Mode profiles for different σ_G^S at resonance.

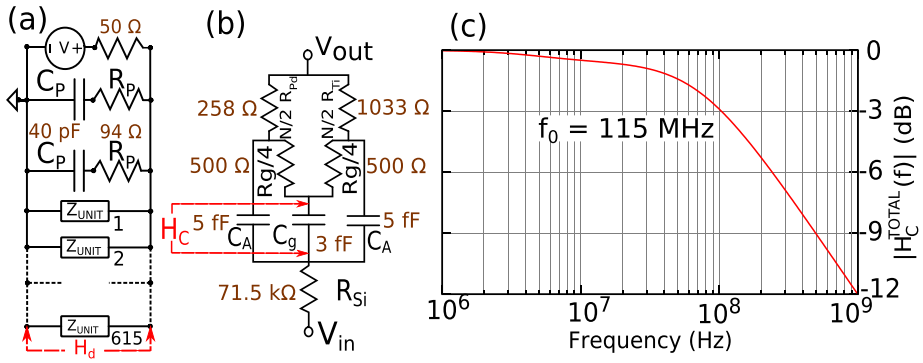

FIG. 3. Lumped element circuit model of the device. (a) Total device circuit. (b) Circuit for a unit cell, Z_{UNIT}. (c) Transfer function across the graphene capacitor, for the total device circuit. H_d is the transfer function across the device, and H_c is the transfer function across the graphene capacitors. $H_C^{TOTAL} = H_c \times H_d$.

UK), a broadband THz source. The sample was biased at its Dirac point (lowest conductivity). The resonance agrees well with graphene sheet conductivity between 0.1 and 0.5 mS, which is consistent with graphene grown under the same conditions and processed in a similar procedure as in Refs. 27 and 28. Figure 2(d) shows electric field mode profiles for the antenna gap which decrease in intensity as σ_G^S increases.

The sheet resistance of the graphene on the device cannot be accurately measured. Large contact resistances,[29] non-parallel conductivity, and geometry dependent current paths caused by the tapering of the antennas distort the measurement non-linearly. However, simulations show that modulation is achievable for physically attainable values of graphene sheet conductivity (see Figure S1 in the supplementary material[31]).

To simulate the speed characteristics of the device, a lumped element circuit model as shown in Fig. 3(a) was developed. The equivalent circuit is driven by an AC voltage source with a 50 Ω output impedance. The device is modelled as many parallel elements/impedances, where C_p is the capacitance of the source/drain pads which were calculated to be 40 pF each. R_p is the back gate resistance to each of these pads and was calculated to be 94 Ω by using numerical methods to account for fringing fields. The remaining parallel elements are 615 unit cell impedances Z_{UNIT}. Figure 3(b) shows the Z_{UNIT} sub circuit, consisting of several different elements. R_{Si} is the unit cell resistance through the p-Si substrate, which by using Pouillet's law was calculated to be 71.5 kΩ. C_A and C_g represent a single antenna arm and graphene capacitances, respectively. Both were simulated using COMSOL Multiphysics v 5.1, to account for fringing fields and yielded values of 5 fF and 3 fF, respectively. R_g represents an average graphene resistance for each of the antenna halves and was estimated based on geometry and a value of graphene sheet resistivity of 1 kΩ (measured from large area graphene of a similar device), giving $R_g = 2$ kΩ. R_{Pd} and R_{Ti} have values of 12.6 Ω and 50.4 Ω, respectively, and represent the resistances of the connecting lines between adjacent antennas. Due to the symmetry of the device, a single cell in the middle of a column of antennas (N = 41) is taken as Z_{UNIT}. To solve the full circuit characteristics, the SPICE simulator was employed to solve the AC voltages and currents of the circuit shown in Fig. 3(a). The optical cut-off frequency (f_0) was taken as the −3 dB value of the voltage transferred across the graphene capacitors from the total circuit, and this is related to the electrical cut-off frequency (f_{3dB}) by $f_0 = \sqrt{3} f_{3dB}$. This ensures the optical cut-off frequency is related to the voltage and not the power transferred across the graphene.[28] Figure 3(c) shows the numerical solution for the voltage transfer function across the graphene capacitors giving a f_0 frequency of 115 MHz. This lumped element model is a simplification of the physics involved but does provide an adequate approximation of f_0 for this class of device.[17,27,28] More importantly, such models are useful for determining limiting factors of f_0, which through careful study was found to be the large capacitance of the source/drain pads.

To characterize the optical modulation characteristics of the device, an optical setup as shown schematically in Fig. 4 was used. THz radiation generated from a 2.0 THz single frequency emission QCL was collimated using a 90° off-axis parabolic mirror (OAPM) with an effective focal length (EFL) of 7.5 cm. A Si beam splitter at 45° was placed in the collimated beam path and another 90° OAPM (EFL = 2.54 cm) focused the light through a 1 mm pinhole onto the sample. The peak power of THz radiation incident on the device was estimated to be 81 μW. The reflected light was re-collimated and semi-reflected by the beam splitter onto a large area Golay cell via a final 90° OAPM (EFL = 15 cm). The laser was operated in continuous pulse mode with a 20 kHz repetition rate and 30% duty cycle, which due to the Golay cell's slow response time (~25 ms), appeared as a constant power source. The array with

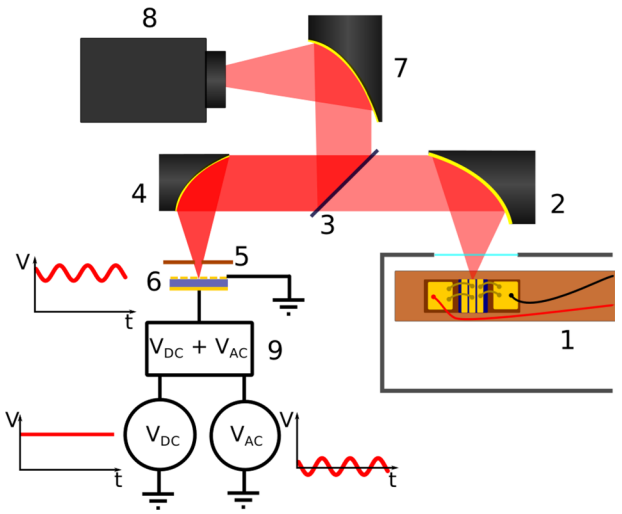

FIG. 4. Optical setup. 1, Single frequency emission 2.0 THz QCL at 4 K. 2, 90° OAPM, EFL = 7.5 cm. 3, Si beam splitter. 4, 90° OAPM, EFL = 2.54 cm. 5, Ø = 1 mm pin hole. 6, Device. 7, 90° OAPM, EFL = 15 cm. 8, Golay Cell detector. 9, Back-gate bias circuit.

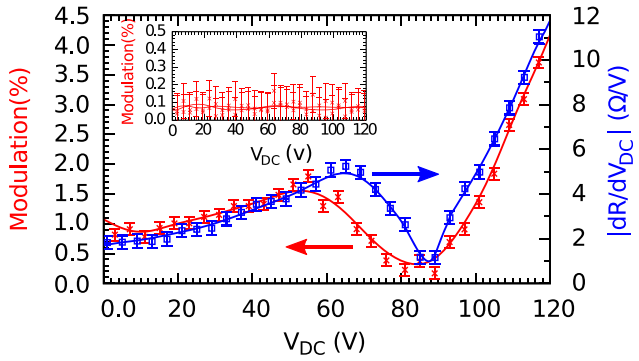

FIG. 5. Optical modulation depth measurement as a function of DC voltage offset V_{DC}. The crosses (×) show the modulated power of THz radiation for a 10 V peak-to-peak square wave at 22 Hz, and the squares (□) show the absolute value of DC differential resistance. The inset shows modulation when the polarization of the THz radiation is perpendicular to the antenna's major axis.

L = 51 μm was chosen as this size of antennas has its resonance peak centered around 2.0 THz. The sample had both source and drain electrodes grounded. The gate voltage $V_G(t)$ was taken as the output from a voltage summing circuit that added a 10 V peak-to-peak square wave with a frequency f_{MOD}, $V_{AC}(f_{MOD}, t)$ to a constant DC value V_{DC}, such that

$$V_G(f_{MOD}, t) = V_{DC} + V_{AC}(f_{MOD}, t). \quad (1)$$

By setting f_{MOD} as 22 Hz, the amplitude of modulation could be measured directly by the Golay cell and lock-in amplifier with the same reference frequency. This method of characterization was chosen because of the superior signal to noise ratio obtained and increased tolerance for thermal and mechanical drift of the optical system. Figure 5 shows the optical modulation depth for THz radiation polarized parallel to the antenna's major axis and the absolute value of the differential resistance as a function of V_{DC}. The minimum differential modulation located around 84 V corresponds to the Dirac point of the device (see Figure S2 in the supplementary material[31]). The modulation depth follows the functional form of the differential resistance, as a higher change in resistance (conductivity) leads to a greater change in reflection, as already observed in Refs. 27 and 28. It is interesting to note that the asymmetry at either side of the Dirac point shows a greater differential resistivity for electrons than for holes, which we attribute to the unintentional doping of graphene during processing and transfer.[30] A modulation depth as high as 4% is achieved with a DC bias of 115 V. The inset shows the modulation for THz radiation polarized perpendicular to the antenna's major axis, which was within the noise floor of the measurement. We note that these values are an underestimate of the actual modulation depth. The size of the pinhole and array is closely matched to maximize signal to noise on the Golay cell. As a result, any spatial mismatch between the two reduces modulated power and, in some cases, can increase absolute reflected power, reducing modulation depth. Finally, the electronics used limited the voltage modulation to 10 V peak-to-peak, preventing the full dynamic range of modulation from been explored.

Owing to the lack of suitably fast detectors sensitive to THz radiation, the speed of the device was estimated by an indirect measurement, as already reported in Refs. 14, 27, and 28. The measurement relies on the non-linear mapping between σ_G^S and the reflectivity. A sinusoidal modulation with a peak-to-peak amplitude of 6 V and frequency f_{MOD} was applied to the back gate. This sinusdal waveform $V_{AC}(f_{MOD}, t)$ is mapped non-linearly to reflection as another periodic waveform $R(f_{MOD}, t)$. The average value of $R(f_{MOD}, t)$ depends on f_{MOD}, and in the limits of high and low frequencies, this average value manifests as two plateaus of power. f_0 is taken as the frequency corresponding to a power half way in between these two plateaus. To improve the sensitivity of the measurement, due to the small change in average value expected, the gate was held at 113 V and $V_{AC}(f_{MOD}, t)$ applied on top of this. The QCL was operated in continuous pulse mode at 22 Hz and 30% duty cycle so that the power could be measured by the lock-in amplifier and Golay cell. The frequency f_{MOD} was swept bi-directionally from 1 to 800 MHz and a lock-in measurement performed at set frequencies in between, with a suitable dwell time to allow the device to settle. The measurements were repeated several times and at different sweep speeds, dwell times, and lock-in integration times. Figure 6 shows an exemplar measurement performed where the data have been scaled from the low frequency plateau to the high frequency plateau and fit using an equation of the form

$$H(f) = \frac{1}{\sqrt{1 + \left(\frac{f}{f_{3dB}}\right)^2}}. \quad (2)$$

f_0 was found to be 105 ± 15 MHz, in very good agreement with the circuit model developed.

In conclusion, we have presented a fast room temperature external optical modulator working at THz frequencies. By reducing the parasitic capacitance from the source/drain pads and optimizing the geometry of the device f_0 frequencies above 10 GHz should be achievable. Several methods to improve the modulation depth of this non-optimized device are possible: Optimized graphene processing and chemical passivation, using top gate dielectrics, would lead to much higher modulation depths, due to a simultaneous reduction of the Dirac point voltage and decrease in homogeneous and

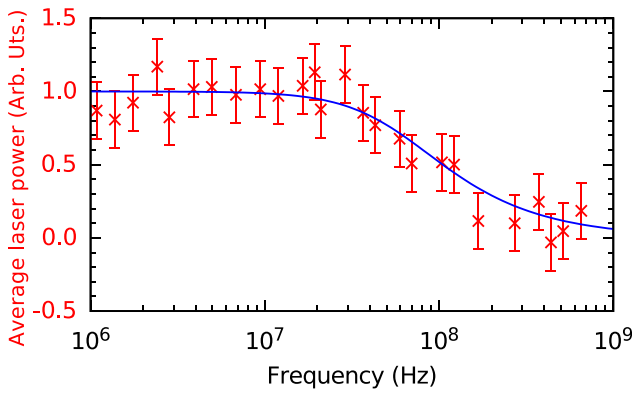

FIG. 6. Normalized optical modulation speed measurement. The blue curve corresponds to the fitting of the data using Equation (2). Each point was acquired with a 500 ms integration time and 3.5 s dwell time.

inhomogeneous broadening of the conductivity/doping. The antenna geometry can be altered to obtain a higher overlap between the optical mode and graphene. Furthermore, the antenna density on the device can be increased further with an overall reduced device size. With such optimizations, it is estimated that modulation depths >25% are feasible, without reducing the device's speed.

R.D., Y.R., H.E.B., and D.A.R. acknowledge financial support from the Engineering and Physical Sciences Research Council (Grant No. EP/J017671/1, Coherent Terahertz Systems). P.B.-W. and S.H. acknowledge financial support from the Engineering and Physical Sciences Research Council (Grant Nos. EP/K016636/1, GRAPHTED). H.L. and J.A.Z. acknowledge financial support from the Engineering and Physical Sciences Research Council (Grant No. EP/L019922/1). Additional data for this article are available at https://www.repository.cam.ac.uk/handle/1810/253533.

[1]A. I. Mcintosh, B. Yang, S. M. Goldup, M. Watkinson, and R. S. Donnan, "Terahertz spectroscopy: A powerful new tool for the chemical sciences?," Chem. Soc. Rev. **41**(6), 2072–2082 (2012).
[2]P. Dean, Y. L. Lim, A. Valavanis, R. Kliese, M. Nikolić, S. P. Khanna, M. Lachab, D. Indjin, Z. Ikonić, P. Harrison, A. D. Rakić, E. H. Linfield, and A. G. Davies, "Terahertz imaging through self-mixing in a quantum cascade laser," Opt. Lett. **36**(13), 2587–2589 (2011).
[3]Y. Ren, R. Wallis, D. S. Jessop, R. Degl'Innocenti, A. Klimont, H. E. Beere, and D. A. Ritchie, "Fast terahertz imaging using a quantum cascade amplifier," Appl. Phys. Lett. **107**, 011107 (2015).
[4]J. F. Federici, B. Schulkin, F. Huang, D. Gary, R. Barat, F. Oliveira, and D. Zimdars, "THz imaging and sensing for security applications—explosives, weapons and drugs," Semicond. Sci. Technol. **20**(7), S266 (2005).
[5]C. Yu, S. Fan, Y. Sun, and E. Pickwell-Macpherson, "The potential of terahertz imaging for cancer diagnosis: A review of investigations to date," Quant. Imaging Med. Surg. **2**(1), 33–45 (2012).
[6]I. F. Akyildiz, J. M. Jornet, and C. Han, "Terahertz band: Next frontier for wireless communications," Phys. Commun. **12**, 16–32 (2014).
[7]S. Koenig, D. Lopez-Diaz, J. Antes, F. Boes, R. Henneberger, A. Lauther, A. Tessmann, R. Schmogrow, D. Hillerkuss, R. Palmer, T. Zwick, C. Koos, W. Freude, O. Ambacher, J. Leuthold, and I. Kallfass, "Wireless sub-THz communication system with high data rate," Nat. Photonics **7**, 977–981 (2013).
[8]H.-J. Song, K. Ajito, Y. Muramoto, A. Wakatsuki, T. Nagatsuma, and N. Kukutsu, "24 Gbit/s data transmission in 300 GHz band for future terahertz communications," Electron. Lett. **48**(15), 953–954 (2012).
[9]K. I. Bolotin, K. J. Sikes, Z. Jiang, M. Kilma, G. Fudenberg, J. Hone, P. Kim, and H. L. Stormer, "Ultrahigh electron mobility in suspended graphene," Solid State Commun. **146**(9–10), 351–355 (2008).
[10]J. Ye, M. F. Craciun, M. Koshino, S. Russo, S. Inoue, H. Yuan, H. Shimotani, A. F. Morpurgo, and Y. Iwasa, "Accessing the transport properties of graphene and its multilayers at high carrier density," Proc. Natl. Acad. Sci. **108**(32), 13002–13006 (2011).
[11]R. Degl'Innocenti, D. S. Jessop, Y. D. Shah, J. Sibik, J. A. Zeitler, P. R. Kidambi, S. Hofmann, H. E. Beere, and D. A. Ritchie, "Low-bias terahertz amplitude modulator based on split-ring resonators and graphene," ACS Nano **8**(3), 2548–2554 (2014).
[12]R. Yan, B. Sensale-Rodriguez, L. Liu, D. Jena, and H. Xing, "A new class of electrically tunable metamaterial terahertz modulators," Opt. Express **20**, 28664–28671 (2012).
[13]B. Sensale-Rodriguez, R. Yan, M. M. Kelly, T. Fang, K. Tahy, W. S. Hwang, D. Jena, L. Liu, and H. G. Xing, "Broadband graphene terahertz modulators enabled by intraband transitions," Nat. Commun. **3**, 780 (2012).
[14]G. Liang, X. Hu, X. Yu, Y. Shen, L. H. Li, A. G. Davies, E. H. Linfield, H. K. Liang, Y. Zhang, S. F. Yu, and Q. J. Wang, "Integrated terahertz graphene modulator with 100% modulation depth," ACS Photonics **2**(11), 1559–1566 (2015).
[15]R. A. Shelby, D. R. Smith, and S. Schultz, "Experimental verification of a negative index of refraction," Science **292**(5514), 77–79 (2001).
[16]S. Linden, C. Enkrich, M. Wegener, J. Zhou, T. Koschny, and C. M. Soukoulis, "Magnetic response of metamaterials at 100 terahertz," Science **306**(5700), 1351–1353 (2004).
[17]Y. Yao, M. A. Kats, R. Shankar, Y. Song, J. Kong, M. Loncar, and F. Capasso, "Wide wavelength tuning of optical antennas on graphene with nanosecond response time," Nano Lett. **14**(1), 214–219 (2014).
[18]Y. Yao, M. A. Kats, P. Genevet, N. Yu, Y. Song, J. Kong, and F. Capasso, "Broad electrical tuning of graphene-loaded plasmonic antennas," Nano Lett. **13**(3), 1257–1264 (2013).
[19]Y. Yao, R. Shankar, M. A. Kats, Y. Song, J. Kong, M. Loncar, and F. Capasso, "Electrically tunable metasurface perfect absorbers for ultrathin mid-infrared optical modulators," Nano Lett. **14**(11), 6526–6532 (2014).
[20]P. R. Kidambi, C. Ducati, B. Blubak, D. Gardiner, R. S. Weatherup, M.-B. Martin, P. Sensor, H. Coles, and S. Hofmann, "The parameter space of graphene chemical vapor deposition on polycrystalline Cu," J. Phys. Chem. C **116**(42), 22492–22501 (2012).
[21]P. R. Kidambi, B. C. Bayer, R. Blume, Z.-J. Wang, C. Baehtz, R. S. Weatherup, M.-G. Willinger, R. Schloegl, and S. Hofmann, "Observing Graphene Grow: Catalyst–Graphene Interactions during Scalable Graphene Growth on Polycrystalline Copper," Nano Lett. **13**(10), 4769–4778 (2013).
[22]T. Mueller, F. Xia, and P. Avouris, "Graphene photodetectors for high-speed optical communications," Nat. Photonics **4**, 297–301 (2010).
[23]M. A. Ordal, L. L. Long, R. J. Bell, S. E. Bell, R. R. Bell, R. W. Alexander, and C. A. Ward, "Optical properties of the metals Al, Co, Cu, Au, Fe, Pb, Ni, Pd, Pt, Ag, Ti, and W in the infrared and far infrared," Appl. Opt. **22**(7), 1099–1119 (1983).
[24]J. M. Dawlaty, S. Shivaraman, J. Strait, P. George, M. Chandrashekhar, F. Rana, M. G. Spencer, D. Veksler, and Y. Chen, "Measurement of the optical absorption spectra of epitaxial graphene from terahertz to visible," Appl. Phys. Lett. **93**, 131905 (2008).
[25]Z. Liu, A. Boltasseva, R. H. Pedersen, R. Bakker, A. V. Kildishev, V. P. Drachev, and V. M. Shalaev, "Plasmonic nanoantenna arrays for the visible," Metamaterials **2**(1), 45–51 (2008).
[26]L. Razzari, A. Toma, M. Clerici, M. Shalaby, G. Das, C. Liberale, M. Chirumamilla, R. P. Zaccaria, F. De Angelis, M. Peccianti, R. Morandotti, and E. Di Fabrizio, "Terahertz dipole nanoantenna arrays: Resonance characteristics," Plasmonics **8**(1), 133–138 (2013).
[27]R. Degl'Innocenti, D. S. Jessop, C. W. O. Sol, L. Xiao, S. J. Kindness, H. Lin, J. A. Zeitler, P. Braeuninger-Weimer, S. Hofmann, Y. Ren, V. S. Kamboj, J. P. Griffiths, H. E. Beere, and D. A. Ritchie, "Fast modulation of terahertz quantum cascade lasers using graphene loaded plasmonic antennas," ACS Photonics **3**(3), 464–470 (2016).
[28]D. S. Jessop, C. W. O. Sol, L. Xiao, S. J. Kindness, P. Braeuninger-Weimer, H. Lin, J. Griffiths, Y. Ren, V. S. Kamboj, C. X. Ren, S. Hofmann, J. A. Zeitler, H. E. Beere, D. A. Ritchie, and R. Degl'Innocenti, "Fast terahertz optoelectronic amplitude modulator based on plasmonic metamaterial antenna arrays and graphene," Proc. SPIE **9747**, 97471E (2016).
[29]S. Russo, M. F. Craciun, M. Yamamoto, A. F. Morpurgo, and S. Tarucha, "Contact resistance in graphene-based devices," Physica E **42**(4), 677–679 (2010).
[30]D. B. Farmer, R. Golizadeh-Mojarad, V. Perebeinos, Y.-M. Lin, G. S. Tulevski, J. C. Tsang, and P. Avouris, "Chemical doping and electron−hole conduction asymmetry in graphene devices," Nano Lett. **9**(1), 388–392 (2008).
[31]See supplementary material at http://dx.doi.org/10.1063/1.4947596 for an additional simulation of reflectivity at resonance (Figure S1) and measured graphene resistance (Figure S2).